immunological reactions play a role in the pathogenesis of endometriosis. In the present study, we focused on the effects of exposure to DE on allergic reactions associated with endometriosis and analyzed them using a rat endometriosis model.

MATERIALS AND METHODS

Animals and Treatments —— Pregnant Sprague-Dawley rats were purchased from Japan SLC, Inc. (Shizuoka, Japan). Four of these rats were exposed to DE through the airway starting on gestational day (GD) 2 and four others were used for control (no exposure to DE). Neonatal rats from the DE-exposed pregnants were exposed to DE until 7 weeks of age (DE exposure group), whereas neonatal rats from the control group were maintained in clean air. Endometriosis was induced in female pups at 8 weeks of age. A 5-mm × 5-mm piece of uterine tissue was attached to each side of the peritoneum by surgical autotransplantation. Induced endometriotic lesions (n = 2 per rat) and blood were obtained from anesthetized rats of the DE exposure group on days 4 (n = 4), 7 (n = 4), and 14 (n = 4) after autotransplantation and from those of the control group on days 4 (n = 4), 7 (n = 4), and 14 (n = 3). Normal peritoneal tissues were also obtained from nontreated rats on days 4 (n = 4), 7 (n = 4), and 14 (n = 3). All animals were handled in accordance with institutional and national guidelines for the care and use of laboratory animals.

DE Exposure —— Rats were exposed to DE 7 hr per day, 5 days per week, in an inhalation chamber at the Research Institute of Tuberculosis, Japan Anti-Tuberculosis Association (Tokyo, Japan). A 2369-cc diesel engine (Isuzu Automobile, Inc., Tokyo, Japan) was operated at 1050 rpm and 80% load with commercial diesel oil. The exhaust was introduced into a stainless steel dilution tunnel and mixed with clean air that was passed through a high-efficiency particulate air filter and a charcoal filter. The concentration of DEPs was adjusted to approximately 1.0 mg DEP/m^3.

Light Microscopic Analysis —— Tissue samples were fixed in formaldehyde-glutaraldehyde fixative (4% formaldehyde and 1% glutaraldehyde in 0.1 M phosphate-buffered saline; pH 7.4). Fixed tissues were washed with phosphate buffer (pH 7.4), dehydrated in a graded series of ethanol, and embedded in paraffin. Paraffin-embedded tissue sections were stained with hematoxylin and eosin (HE) for histologic analysis.

Serum Monocyte Chemoattractant Protein (MCP)-1 Level —— Serum MCP-1 level was measured with the use of a commercially available ELISA kit (Biosource Inc., Camarillo, CA, U.S.A.) according to the manufacturer's instructions.

Statistical Analysis —— Data are shown as mean ± standard error of the mean (SEM). Unpaired t-test was used to analyze differences in values between two groups. A p value of <0.05 was considered statistically significant.

RESULTS

Effect of DE Exposure on Litter Size, Sex Ratio and Body Weight of Pups

Eight pregnant rats in this study delivered their pups on GD 22. There was no significant difference in litter size and sex ratio of pups between the DE exposure group and the control group. Body weight of female pups in the DE exposure group was significantly lower than that in the control group when the pups were 4 days old and 8 weeks old (Table 1).

Effect of DE Exposure on Changes in Histopathologic Features

In rats, the abdominal wall is made up of three muscles, the internal abdominal muscle, which is nearest the abdominal cavity, the medial abdominal muscle, and the external abdominal muscle (Fig. 1 A). Analysis of which abdominal muscles have been affected by interstitial stromal cell hyperplasia, a proliferative lesion, is useful for investigating the pathogenesis of endometriosis.[19] Proliferative stromal lesions in the peritoneum adjacent to the autotransplanted endometrial tissue reached the internal abdominal muscle within 4 days after autotransplantation (Fig. 1B). The lesions reached their maximum extent within 7 days (Fig. 1C), and they were decreased on day 14 (Fig. 1D, E). Endometriotic lesions induced in the

Table 1. Body Weight of Female Pups in the DE Exposure and Control Groups

	Control group	DE exposure group
4 days old	7.7 ± 0.2 g (n = 23)	6.4 ± 0.4 g (n = 22)**
3 weeks old	35.8 ± 0.8 g (n = 23)	36.3 ± 0.6 g (n = 21)
8 weeks old	201.8 ± 3.3 g (n = 12)	187.5 ± 1.9 g (n = 12)**

Data are mean ± SEM. **Statistically significant difference between two groups ($p < 0.01$).

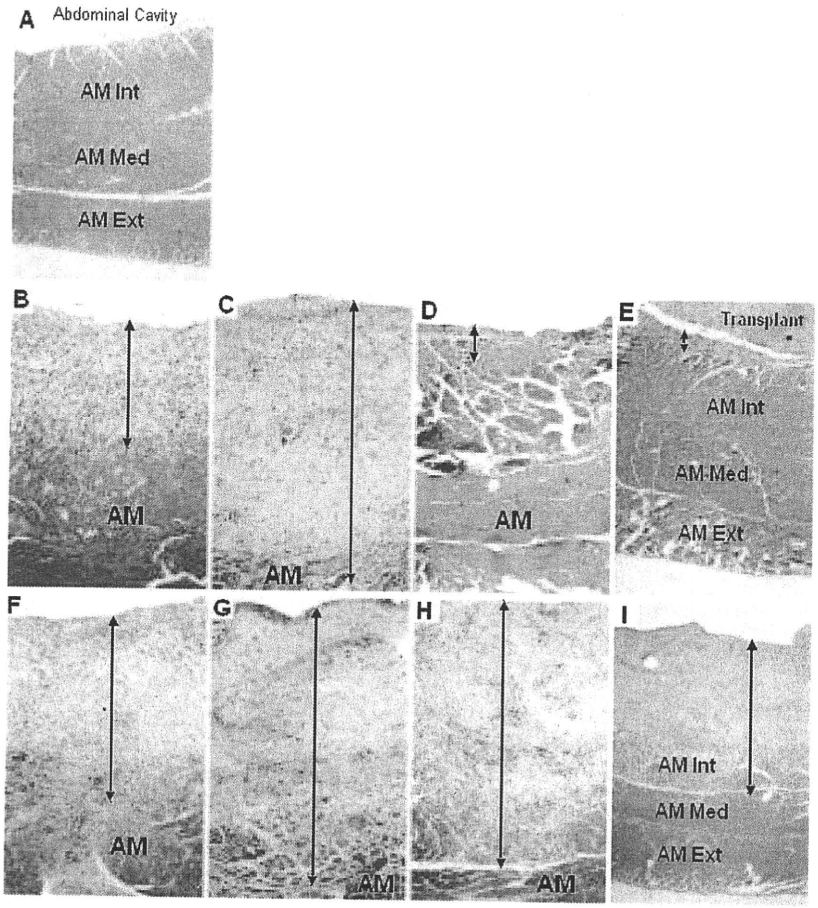

Fig. 1. Histopathological Features of the Rat Endometriosis Model in the DE Exposure Group and Control Group

HE-stained images show normal peritoneal tissue (A), and endometriosis model in rats of the control group on days 4 (B), 7 (C), and 14 (D and E) after autotransplantation and of the DE exposure group on days 4 (F), 7 (G), and 14 (H and I). AM, abdominal muscle; Int, internal; Med, medial; Ext, external; Magnification: B–D, F–H, and J, × 100; A, E, and I, × 40. Double-headed arrows indicate proliferative lesions.

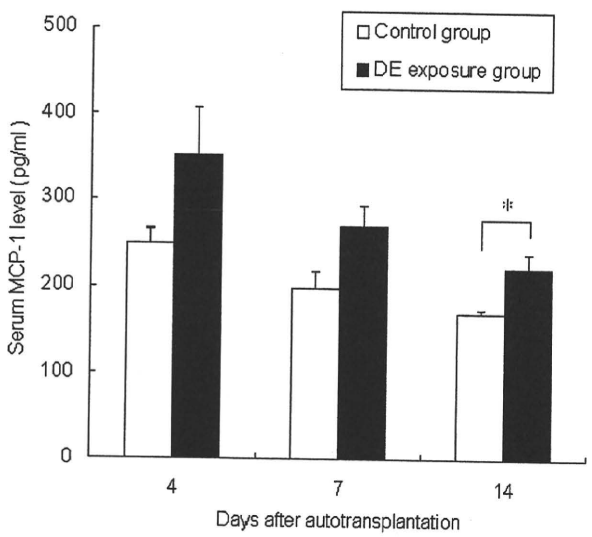

Fig. 2. Effects of DE Exposure on Serum MCP-1 Level in Rat Endometriosis Model

Serum MCP-1 levels were analyzed with ELISA. Data are mean ± SEM. *Statistically significant difference in the serum MCP-1 level between two groups ($p < 0.05$).

DE exposure group did not differ from those induced in the control group on days 4 and 7 after autotransplantation (Fig. 1F, G), but proliferative lesions in the DE exposure group had reached to the medial abdominal muscle by day 14 (Fig. 1H–J). To reveal the effect of DE more clearly, we measured the thickness of the proliferative lesions on day 14. The thickness of the lesions increased by a factor of 7.7 times in the DE exposure group compared to that in the control group on day 14.

Effects of DE Exposure on Serum MCP-1 Level in Rat with Endometriosis Model

The serum MCP-1 level of rats with endometriosis was significantly higher in the DE exposure group than in the control group on day 14 ($p < 0.05$) (Fig. 2).

DISCUSSION

A number of factors contribute to the pathogenesis of endometriosis. Although critical factors for the pathogenesis were not determined, we focused on the contribution of immunological factors because increase of activated mast cells has been observed in the rat endometriosis model[19] and in human endometriosis,[21] and the rat model was reduced by the effect of leukotriene antagonist.[22] In the present study, we analyzed the effects of DE exposure on histologic features and serum MCP-1 level in a rat endometriosis model.

Body weight of female pups in the DE exposure group was significantly lower than that in the control group. This weight loss corresponded with those of previous reports.[7,23] Recent studies reported that some components of DE, for example, carbon monoxide and sulfur oxides, induce weight loss in rats[24] and in humans.[25] The decreased body weight observed in the present study could be induced by these components.

Endometriosis was induced in female pups at 8 weeks of age. Proliferative stromal lesions reached the internal abdominal muscle by day 4 after uterine autotransplantation, and were decreased by day 14 in the control rats. In contrast, proliferative lesions reached the medial abdominal muscle on day 14 in the DE exposure group. This observation suggests that DE exposure enhance the persistence of this rat endometriosis model.

Serum MCP-1 level is increased in rats with endometriosis in comparison to those without endometriosis.[20] Several clinical researchers reported that serum MCP-1 is higher in women with endometriosis than in those without[26–28] and suggested its usefulness as a biomarker for nonsurgical prediction of endometriosis in humans.[29] Gmyrek *et al.*[27] reported that serum MCP-1 level in women with endometriosis was correlated with severity of the disease. In the present study, we showed that the serum MCP-1 level of rats with endometriosis was significantly increased in the DE exposure group relative to that in the control group on day 14 after autotransplantation ($p < 0.05$). This finding supports the histologic observation of persistence of the endometriosis model in the DE exposure group.

In summary, DE exposure enhances the persistence of proliferative stromal lesions of rat endometriosis model and increases serum MCP-1 level in rats with endometriosis. Present results suggest that DE exposure exaggerates the pathology of endometriosis and that it may contribute to the increasing prevalence of this disease.

Acknowledgements We thank Dr. I. Sugawara and Mr. T. Udagawa (Research Institute of Tuberculosis) for help with DE exposure, and the students in Takeda Laboratory, especially Ms. R. Fujimoto, Ms. T. Komatsu, Mr. N. Moriya, Ms. M. Iwata, Ms. M. Shimizu, Mr. Y. Takahashi, Mr. S. Yokota, Ms. T. Sugiyama, Mr. T. Oba, Ms. Y. Okada, and Mr. A. Sato for technical assistance.

REFERENCES

1) Garshick, E., Laden, F., Hart, J. E., Rosner, B., Smith, T. J., Dockery, D. W. and Speizer, F. E. (2004) Lung cancer in railroad workers exposed to diesel exhaust. *Environ. Health Perspect.*, **112**, 1539–1543.
2) Hart, J. E., Laden, F., Schenker, M. B. and Garshick, E. (2006) Chronic obstructive pulmonary disease mortality in diesel-exposed railroad workers. *Environ. Health. Perspect.*, **114**, 1013–1017.
3) Mills, N. L., Törnqvist, H., Gonzalez, M. C., Vink, E., Robinson, S. D., Söderberg, S., Boon, N. A., Donaldson, K., Sandström, T., Blomberg, A. and Newby, D. E. (2007) Ischemic and thrombotic effects of dilute diesel-exhaust inhalation in men with coronary heart disease. *N. Engl. J. Med.*, **357**, 1075–1082.
4) Mills, N. L., Törnqvist, H., Robinson, S. D., Gonzalez, M., Darnley, K., MacNee, W., Boon, N. A., Donaldson, K., Blomberg, A., Sandstrom, T. and Newby, D. E. (2005) Diesel exhaust inhalation causes vascular dysfunction and impaired endogenous fibrinolysis. *Circulation*, **112**, 3930–3936.
5) Peters, A., von Klot, S., Heier, M., Trentinaglia, I., Hörmann, A., Wichmann, H. E., Löwel, H. and Cooperative Health Research in the Region of Augsburg Study Group (2004) Exposure to traffic and the onset of myocardial infarction. *N. Engl. J. Med.*, **351**, 1721–1730.
6) Törnqvist, H., Mills, N. L., Gonzalez, M., Miller, M. R., Robinson, S. D., Megson, I. L., Macnee, W., Donaldson, K., Söderberg, S., Newby, D. E., Sandström, T. and Blomberg, A. (2007) Persistent endothelial dysfunction in humans after diesel exhaust inhalation. *Am. J. Respir. Crit. Care Med.*, **176**, 395–400.
7) Ono, N., Oshio, S., Niwata, Y., Yoshida, S., Tsukue, N., Sugawara, I., Takano, H. and Takeda, K. (2007) Prenatal exposure to diesel exhaust impairs mouse

spermatogenesis. *Inhal. Toxicol.*, **19**, 275–281.
8) Yoshida, M., Yoshida, S., Sugawara, I. and Takeda, K. (2002) Maternal exposure to diesel exhaust decreases expression of steroidogenic factor-1 and Müllerian inhibiting substance in the murine fetus. *J. Health Sci.*, **48**, 317–324.
9) Yoshida, S., Ono, N., Tsukue, N., Oshio, S., Umeda, T., Takano, H. and Takeda, K. (2006) In utero exposure to diesel exhaust increased accessory reproductive gland weight and serum testosterone concentration in male mice. *Environ. Sci.*, **13**, 139–147.
10) Yoshida, S., Sagai, M., Oshio, S., Umeda, T., Ihara, T., Sugamata, M., Sugawara, I. and Takeda, K. (1999) Exposure to diesel exhaust affects the male reproductive system of mice. *Int. J. Androl.*, **22**, 307–315.
11) Tsukue, N., Yoshida, S., Sugawara, I. and Takeda, K. (2004) Effect of diesel exhaust on development of fetal reproductive function in ICR female mice. *J. Health Sci.*, **50**, 174–180.
12) Fujimoto, A., Tsukue, N., Watanabe, M., Sugawara, I., Yanagisawa, R., Takano, H., Yoshida, S. and Takeda, K. (2005) Diesel exhaust affects immunological action in the placentas of mice. *Environ. Toxicol.*, **20**, 431–440.
13) Sugamata, M., Ihara, T., Takano, H., Oshio, S. and Takeda, K. (2006) Maternal diesel exhaust exposure damages newborn murine brains. *J. Health Sci.*, **52**, 82–84.
14) Diaz-Sanchez, D., Jyrala, M., Ng, D., Nel, A. and Saxon, A. (2000) In vivo nasal challenge with diesel exhaust particles enhances expression of the CC chemokines rantes, MIP-1 alpha, and MCP-3 in humans. *Clin. Immunol.*, **97**, 140–145.
15) Diaz-Sanchez, D., Tsien, A., Casillas, A., Dotson, A. R. and Saxon, A. (1996) Enhanced nasal cytokine production in human beings after in vivo challenge with diesel exhaust particles. *J. Allergy Clin. Immunol.*, **98**, 114–123.
16) Matsumoto, A., Hiramatsu, K., Li, Y., Azuma, A., Kudoh, S., Takizawa, H. and Sugawara, I. (2006) Repeated exposure to low-dose diesel exhaust after allergen challenge exaggerates asthmatic responses in mice. *Clin. Immunol.*, **121**, 227–235.
17) Giudice, L. C. and Kao, L. C. (2004) Endometriosis. *Lancet*, **364**, 1789–1799.
18) Sampson, J. A. (1927) Peritoneal endometriosis due to the menstrual dissemination of endometrial tissue into the peritoneal cavity. *Am. J. Obstet. Gynecol.*, **14**, 422–469.
19) Uchiide, I., Ihara, T. and Sugamata, M. (2002) Pathological evaluation of the rat endometriosis model. *Fertil. Steril.*, **78**, 782–786.
20) Umezawa, M., Sakata, C., Tanaka, N., Kudo, S., Tabata, M., Takeda, K., Ihara, T. and Sugamata, M. (2008) Cytokine and chemokine expression in a rat endometriosis is similar to that in human endometriosis. *Cytokine*, in press.
21) Sugamata, M., Ihara, T. and Uchiide, I. (2005) Increase of activated mast cells in human endometriosis. *Am. J. Reprod. Immunol.*, **53**, 120–125.
22) Ihara, T., Uchiide, I. and Sugamata, M. (2004) Light and electron microscopic evaluation of antileukotriene therapy for experimental rat endometriosis. *Fertil. Steril.*, **81**, 819–823.
23) Tsukue, N., Tsubone, H. and Suzuki, A. K. (200[illegible] Diesel exhaust affects the abnormal delivery in pregnant mice and the growth of their young. *Inhal. Toxicol.*, **14**, 635–651.
24) Bobak, M. (2000) Outdoor air pollution, low birth weight, and prematurity. *Environ. Health Perspect.*, **108**, 173–176.
25) Yun, D. R. (1975) The effects of chronic exposure to CO-SO_2 mixed gases on the gestation pattern of the rats. *Seoul J. Med.*, **16**, 242–246.
26) Akoum, A., Lemay, A., McColl, S. R., Paradis, I. and Maheux, R. (1996) Increased monocyte chemotactic protein-1 level and activity in the peripheral blood of women with endometriosis. Le Groupe d'Investigation en Gynécologie. *Am. J. Obstet. Gynecol.*, **175**, 1620–1625.
27) Gmyrek, G. B., Sozanski, R., Jerzak, M., Chrobak, A., Wickiewicz, D., Skupnik, A., Sieradzka, U., Fortuna, W., Gabrys, M. and Chelmonska-Soyta, [illegible] (2005) Evaluation of monocyte chemotactic protein-1 levels in peripheral blood of infertile women with endometriosis. *Eur. J. Obstet. Gynecol. Reprod. Biol.*, **122**, 199–205.
28) Pizzo, A., Salmeri, F. M., Ardita, F. V., Sofo, V., Tripepi, M. and Marsico, S. (2002) Behaviour of cytokine levels in serum and peritoneal fluid of women with endometriosis. *Gynecol. Obstet. Invest.*, **54**, 82–87.
29) Othman, E., Hornung, D., Salem, H. T., Khalifa, E. A., El-Metwally, T. H. and Al-Hendy, A. (2008) Serum cytokines as biomarkers for nonsurgical prediction of endometriosis. *Eur. J. Obstet. Gynecol. Reprod. Biol.*, **137**, 240–246.

Applied Surface Science 255 (2008) 1139–1142

Contents lists available at ScienceDirect

Applied Surface Science

journal homepage: www.elsevier.com/locate/apsusc

Interaction between diesel exhaust particles and cellular oxidative stress

K. Suzuki [a,b,*], T. Komatsu [b], M. Kubo-Irie [b], M. Tabata [b], K. Takeda [b], Y. Nihei [a]

[a] Faculty of Science and Technology, Tokyo University of Science, 2641 Yamazaki, Noda-shi, Chiba 278-8510, Japan
[b] Faculty of Pharmaceutical Science, Tokyo University of Science, 2641 Yamazaki, Noda-shi, Chiba 278-8510, Japan

ARTICLE INFO

Article history:
Available online 8 May 2008

Keywords:
TOF-SIMS
RT-PCR
STEM
Nanoparticle
Oxidative stress
Diesel exhaust particle

ABSTRACT

The cellular oxidative stress by the exposure of diesel exhaust particles (DEPs) was investigated by using a time of flight secondary ion mass spectrometry (TOF-SIMS) and a real time reverse transcription polymerase chain reaction (RT-PCR) and a scanning transmission electron microscope (STEM). The DEP surfaces which had different properties were prepared for examining the oxidative stress by a gas chromatography mass spectrometry (GC–MS). We characterized the compositions in the different DEP surfaces and measured the gene expression of heme oxygenase-1 (HO-1) which were induced for preventing the cellular oxidative stress. From these results, it was clear that the DEP compositions (Fe, etc.) correlated closely with the cellular oxidative stress. From the results of a STEM analysis, we found out that the DEP were taken up in the cell and that some mitochondria in close association to the DEP showed damaged morphology. Moreover, the iron oxide nanoparticles of several nanometer were aggregated in the DEP. We therefore concluded that there was the interaction between the cellular functions and the particle properties.

1. Introduction

Recently, many researchers of toxicology and pathology have stated that the diesel exhaust particles (DEPs) emitted from diesel engines have a negative influence on the respiratory, male reproductive functions and central nervous systems [1–3]. Particularly, it became clear that the DEP (including diesel exhaust nanoparticles) had the possibility to bring about not only a lung cancer and a bronchial asthma but also endocrine disruptors. However, Mauderly et al. and Gallagher et al. have found that the exposure of carbon black particles (CBPs) and titanium dioxide particles (TiO_2 particles), both of which were non-toxic and devoid of genotoxic polycyclic aromatic hydrocarbons (PAHs) caused a lung tumour [4,5]. It is desirable to make clear which the kinds of chemical compositions on the DEP surfaces are harmful to human health.

Another problem with the toxicity of the nanoparticles such as CBP, TiO_2 particles, and DEP is that the difference of this toxic mechanism are not elucidated [6,7]. Wittmaack at GSF-National Research Center have reported that the adverse health effects by the nanoparticles exposure was associated with the nanoparticle properties of both chemical compositions and surface area [6]. In the atmospheric environment, many nanoparticles with various compositions and size are suspended [8]. Therefore, it is necessary to investigate the physical and chemical properties of the nanoparticles, i.e. particle diameter, surface area, and composition which will have the biological responses, i.e. oxidative stress, DNA damage, and uptake of the nanoparticles.

We have investigated whether nanosize particles were transported to each organ after the nanoparticles exposure in mice. It was found that various nanoparticles reached to each organ by the blood, and were taken up into the cells; these facts suggested that we could understand how the nanoparticles have a fatal influence on a human body. Hence, it is important to analyze the interaction between the cellular functions and the nanoparticle properties for the discussion of the nanoparticles exposure.

2. Experimental

2.1. Oxidative stress measurement

Generally, related to cellular oxidative stress by the DEP exposure, the reactive oxygen species (ROS) play an important rule in the various diseases, such as cancer and injury [9,10]. The ROS produce at the DEP surfaces in vitro and in vivo [9,10]. Especially, iron is very important because it has the ability to generate the ROS via Fenton chemistry [1]. For example, Sagai et al. have reported

* Corresponding author at: Faculty of Science and Technology, Tokyo University of Science, 2641 Yamazaki, Noda-shi, Chiba 278-8510, Japan.
E-mail address: k.suzuki21@gmail.com (K. Suzuki).

0169-4332/$ – see front matter © 2008 Elsevier B.V. All rights reserved.
doi:10.1016/j.apsusc.2008.05.038

that the macrophages in the lung which were treated with the DEP generated the ROS such as superoxide (O_2^-) and hydroxyl radicals (•HO) and that the superoxide (O_2^-) were reduced to the hydroxyl radicals (•HO) by the catalysis of iron which were included in the DEP [1]. Thus, produced hydroxyl radicals (•HO) causes DNA damages. According to the report of the interaction between soot and iron particles [11], it has been suggested that the soot coexisting with the iron particles had a large influence to the oxidative stress in vivo. Thus, it is necessary to characterize iron in the DEP surfaces and to measure the cellular oxidative stress.

In this study, the DEP compositions were determined using a time of flight secondary ion mass spectrometry (TOF-SIMS). The oxidative stresses of cultured cells by the DEP exposure were measured using a real time reverse transcription polymerase chain reaction (RT-PCR) in vitro. The single cell analysis was performed using a scanning transmission electron microscope (STEM).

2.2. Preparation of washed DEP by GC–MS

The diesel exhaust particles which were removed from the organic matter adsorbed on the DEP surfaces (washed DEP or WDEP) were prepared for examining the gene expression in the cultured cells. A 50 mg portion of the DEP were dispersed in toluene (10 ml, Wako pure chemical industries, Ltd.) for an hour using an ultra sonic washer (UT-105S, Sharpe Co.) and washed it four times in total changing the toluene. The decrease rates of extracted organic matter were calculated from the peak intensities using a gas chromatography mass spectrometry (GC-MS-QP2010, Shimadzu). The amounts of adsorbed organic matter on the DEP surfaces were determined from the decrease rates (Fig. 1).

We found out that the washing time of 46 min was needed to remove the organic matter of 50%. Hence, we prepared the WDEP which were washed for 46 min. The WDEP (washing time: 46 min or 4 h) were dried to remove the toluene at 150 °C. The DEP were collected from an exhaust pipe of a diesel-powered vehicle.

2.3. Particle surface analysis by TOF-SIMS

A TOF-SIMS analysis was carried out using a TRIFT™ 2 apparatus (ULVAC-PHI Inc.) for detecting each particle (DEP or WDEP) compositions. Each particle was placed on the silicon wafer with condensed condition and was measured at the analyzed area (100 μm × 100 μm) while monitoring secondary ion images. The operating conditions of the TOF-SIMS were a beam diameter (image resolution) of about 3 μm, an accelerating voltage of 15 kV,

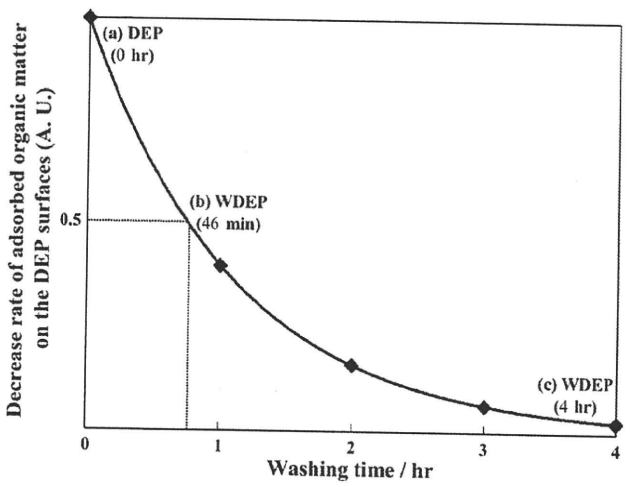

Fig. 1. Decreased rate of adsorbed organic matter on the DEP surfaces by a GC–MS.

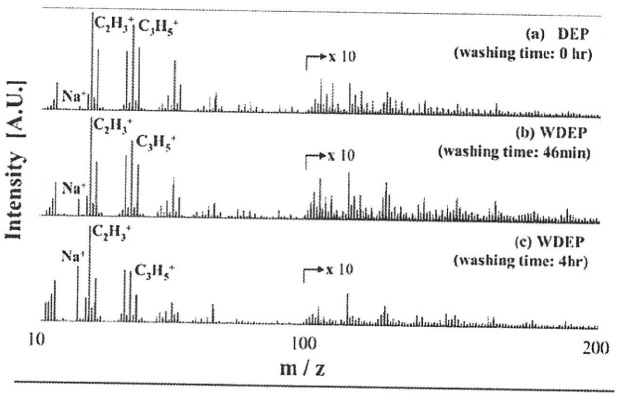

m / z	Secondary Ion	Secondary Ion Intensity [counts]		
		(a) DEP (0 hr)	(b) WDEP (46 min)	(c) WDEP (4 hr)
27.023	$C_2H_3^+$	134874 (0.27)	90929 (0.33)	51261 (0.44)
41.039	$C_3H_5^+$	155458 (0.25)	86013 (0.34)	38015 (0.51)
22.990	Na^+	5417 (1.4)	14760 (0.82)	28257 (0.59)
39.963	Ca^+	1319 (2.8)	2039 (2.2)	3992 (1.6)
55.935	Fe^+	1216 (2.9)	2697 (1.9)	6154 (1.3)

*(systematic error: %)

Fig. 2. TOF-SIMS analysis of each type of diesel exhaust particles (DEPs).

and a primary ion source of gallium. A electron gun was used to prevent charging up.

2.4. Nanoparticle exposure assay by RT-PCR

The Leydig cells (TM3 cells) were cultured in a 60 mm dish for 2 days and were exposed to 30, 100 μg/ml of the DEP (WDEP) for 48 h. The TM3 cells which were exposed to the DEP were washed by phosphate buffered saline (PBS) enough. Total RNA were extracted from the TM3 cells using a ISOGEN (Nippon gene Co., Ltd.). A 1 μg portion of the RNA was dispersed in water (16 μg) and added a DNase (Promega Co.) and a reverse transcriptase (M-MLV, Invitrogen Co.) to perform the RT-PCR. A Random Primer (Takara bio Inc.) was used for the amplification of complementary DNA

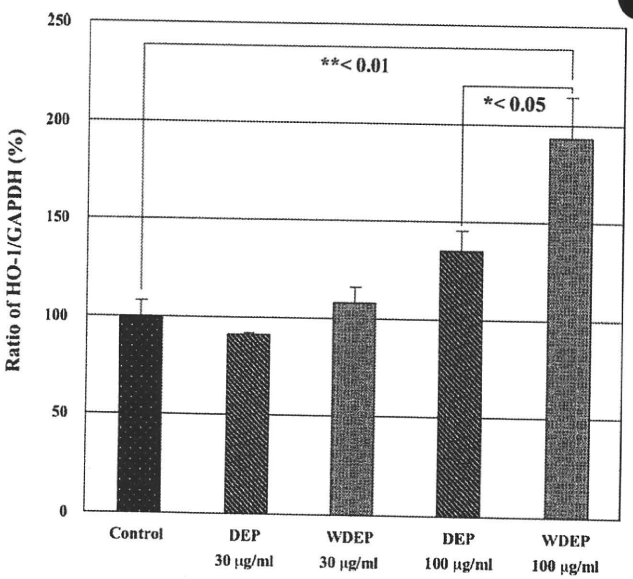

Fig. 3. The gene expression of HO-1 in the TM3 cell.

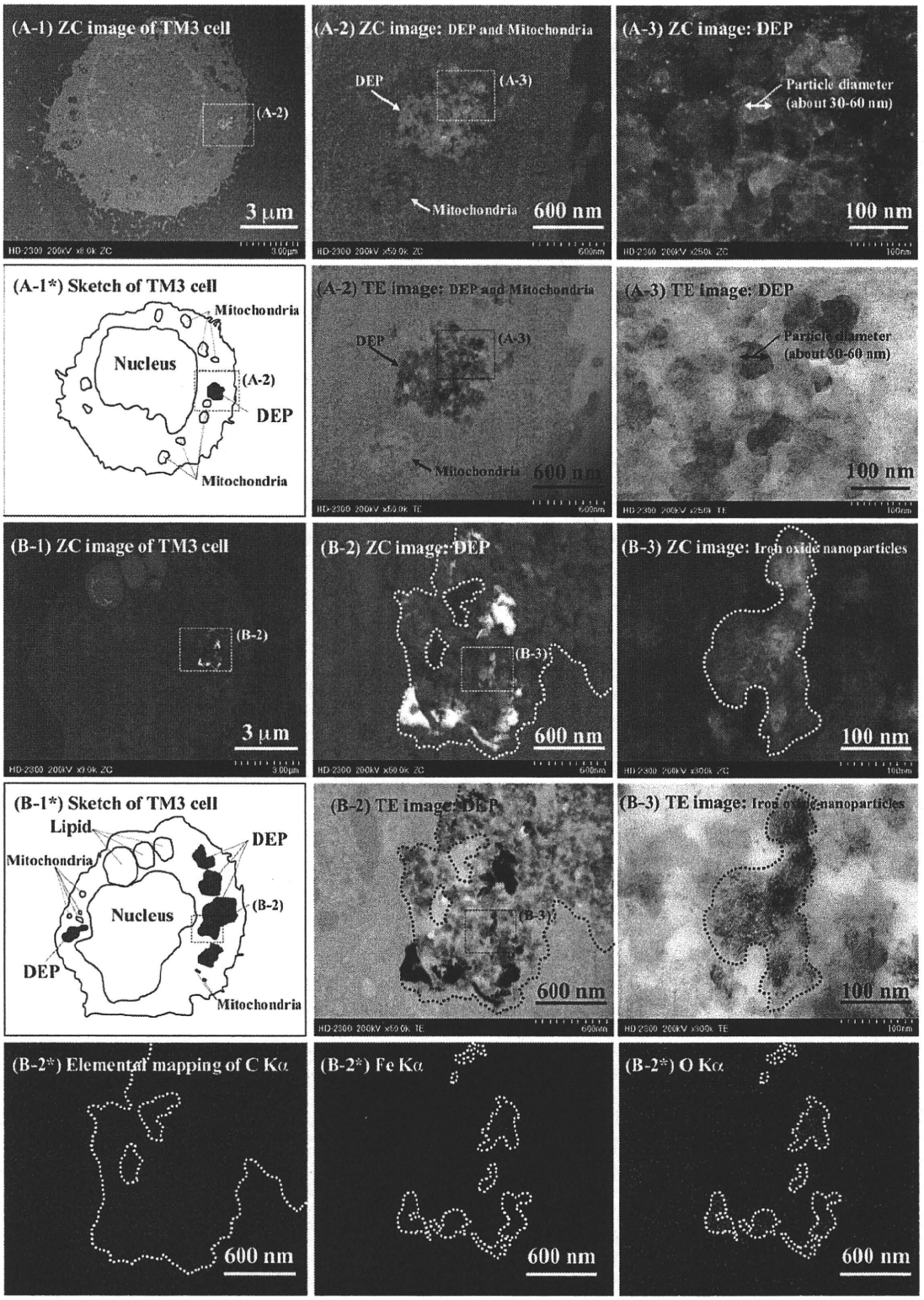

Fig. 4. Identification of diesel exhaust particles in TM3 cell using STEM/EDS.

(cDNA). For the investigation of oxidative stress by the DEP exposure, the gene expression of heme oxygenase-1 (HO-1) which were induced for preventing cellular oxidative stress in the TM3 cells were measured by using a real time RT-PCR (ABI PRISM 7700, Applied Biosystems, Japan) [12]. A glyceraldehydes 3 phosphate dehydrogenase (GAPDH) was used as an endogenous control.

2.5. Single cell analysis by STEM/EDS

The cultured cells which were exposed to the DEP were embedded in epoxy resin for STEM observations. These samples were cut with thickness of about 80 nm using an Ultra-Microtome (Leica EM UC6rt, Leica Microsystems, Japan). The ultra-thin sections

were put on a TEM grid (Cu 150-B, Okenshoji Co., Ltd.) and were analyzed using a STEM/EDS (HD-2300, Hitachi High-technology Co.). We investigated the DEP information of particle diameter, composition, and internal position in the TM3 cell. A Z-contrast (ZC) images which were reflected an atomic number and transmission electron (TE) images were used for the cell observations. The DEP in the TM3 cell were identified from an elemental mapping using an energy dispersive X-ray spectroscopy (EDS).

3. Results and discussion

3.1. Particle surface analysis by TOF-SIMS

The TOF-SIMS spectra and the secondary ion intensities of characteristic peaks at each DEP surfaces (a–c) were shown in Fig. 2. From the results of TOF-SIMS measurements, the secondary ion intensities of fragment peaks ($C_2H_3^+$, $C_3H_5^+$) were reduced at the ratio of about 50%. On the other hand, the secondary ion intensities of sodium, calcium, and iron were increasing, inversely. The fragment pattern (mass range: 100–200) resembled each other. Hence, there was the possibility of that the intensities of Na^+, Ca^+, Fe^+ came from the particle cores because the organic matter on the DEP surfaces were removed. Thus, we could make the DEP surfaces which had the different particle properties to investigate the effect of the oxidative stress in the TM3 cells.

3.2. Nanoparticle exposure assay by RT-PCR

The gene expression of HO-1 in TM3 cells which exposed the DEP (a) and the WDEP (c) were shown in Fig. 3. When we compared 30 μg/ml of the DEP (a) with one of the WDEP (c), these results did not have a significant difference. However, 100 μg/ml of the WDEP (c) were increasing about the gene expression of HO-1 as compared with the control. This result indicates that the WDEP correlate closely with the oxidative stress because the gene expression of HO-1 were induced for preventing the cellular oxidative stress [12]. Moreover, the gene expression by the WDEP (c) exposure was higher than one by the DEP (a) exposure. It seemed that these results were caused by the difference of the particle properties of compositions (Fe) (Fig. 2). Hence, we concluded that there was the interaction between the oxidative stress and composition.

3.3. Single cell analysis by STEM/EDS

The ZC images of the characteristic single cell (A-1, B-1) and the sketches of the cell (A-1*, B-1*) were shown in Fig. 4. The detail images (ZC images and TE images) also were shown in Fig. 4 (A-2, A-3, and B-2, B-3). From these observations of the TM3 cell which were exposed to the DEP, it became clear that the DEP were taken up in the TM3 cell and that some mitochondria in close association to DEP showed damaged morphology (A-2). Moreover, we found out that the single nanoparticle had 30–60 nm at average diameter (A-3).

The DEP having the different contrasts were taken up in the TM3 cell (B-2). It was considered that these differences of the DEP images reflected the composition of the DEP. From the STEM observations in detail, the fine nanoparticles of several nanometer were aggregated in the DEP (B-3). Moreover, we carried out a X-ray analysis against these fine nanoparticles. From the results of a X-ray analysis, it was found that the characteristic nanoparticles were iron oxide nanoparticles (B-2*). These results corresponded well to the obtained information of the particle cores by a TOF-SIMS analysis. Another important result was that the DEP which were taken up in the cell was able to be identified from the elemental mapping of C Kα (B-2*). It was usually difficult to identify the DEP by a X-ray analysis because C Kα of the cell and it of the DEP overlapped each other.

4. Conclusion

In this study, we investigated the oxidative stress caused by different DEP on TM3 cells using TOF-SIMS, RT-PCR and STEM. From these results of TOF-SIMS and RT-PCR, it was clear that there was the interaction between the oxidative stress and the particle compositions (Fe, etc.). In the STEM analysis, some mitochondria in close association to the DEP showed damaged morphology. It therefore is very important to obtain the detail information about both the cellular functions and the nanoparticle properties.

Acknowledgements

JSPS Research Fellowships for young scientists supported this work. We wish to acknowledge Mitsubishi Gas Chemical Co. Inc. for cooperation in the TOF-SIMS analysis and STEM measurements. Prof. Masaru Sagai at Aomori University of Health and Welfare, the research group of Prof. Takeda at Science University of Tokyo, Dr. Tomiyasu at The University of Tokyo, and Mr. Kanda at Nihei Laboratory are thanked for useful discussions.

References

[1] T. Ichinose, Y. Yajima, M. Nagashima, S. Takenoshita, Y. Nagamachi, M. Sagai, Carcinogenesis 18 (1997) 185–192.
[2] S. Yoshida, M. Sagai, S. Oshio, T. Umeda, T. Ihara, M. Sugamata, I. Sugawara, K. Takeda, International Journal of Andrology 22 (5) (1999) 307–315.
[3] M. Sugamata, T. Ihara, H. Takano, S. Oshio, K. Takeda, Journal of Health Science 52 (1) (2006) 82–84.
[4] J.L. Mauderly, M.B. Snipes, E.B. Barr, S.A. Belinsky, J.A. Bond, A.L. Brooks, I.Y. Chang, Y.S. Cheng, N.A. Gillett, W.C. Griffith, et al. Research Report (Health Effects Institute) 68 (1994).
[5] J. Gallagher, U. Heinrich, M. George, L. Hendee, D.H. Phillips, J. Lewtas, Carcinogenesis 15 (1994) 1291–1299.
[6] K. Wittmaack, Environmental Health Perspectives 115 (2007) 187–194.
[7] T. Stoeger, C. Reinhard, S. Takenaka, A. Schroeppel, E. Karg, B. Ritter, J.m. Heyder, H. Schulz, Environmental Health Perspectives 114 (2006) 328–333.
[8] N. Fukuhara, K. Suzuki, K. Takeda, Y. Nihei, Applied Surface Science, in press.
[9] Ken Donaldson, Paul Borm, Particle Toxicology, CRC Press, Taylor & Francis Group, 2006, pp. 89–138, 299–316.
[10] C.G. Pam, D.A. Schmitz, A.K. Cho, J. Froines, J.M. Fukuto, Toxicological Sciences 81 (2004) 225–232.
[11] Y.M. Zhou, C.Y. Zhong, I.M. Kennedy, V.J. Leppert, K.E. Pinkerton, Toxicology Applied Pharmacology 190 (2003) 157–169.
[12] N. Li, C. Sioutas, A. Cho, D. Schmitz, C. Misra, J. Sempf, M. Wang, T. Oberley, J. Froines, A. Nel, Environmental Health Perspectives 111 (2003) 455–460.

Applied Surface Science 255 (2008) 1538–1540

Contents lists available at ScienceDirect

Applied Surface Science

journal homepage: www.elsevier.com/locate/apsusc

Characterization of environmental nanoparticles

N. Fukuhara [a,*], K. Suzuki [a], K. Takeda [b], Y. Nihei [a]

[a] Faculty of Science and Technology, Science University of Tokyo, 2641 Yamazaki, Noda-shi, Chiba 278-8510, Japan
[b] Faculty of Pharmaceutical Science, Science University of Tokyo, 2641 Yamazaki, Noda-shi, Chiba 278-8510, Japan

ARTICLE INFO

Article history:
Available online 8 May 2008

Keywords:
TOF-SIMS
SMPS
FE-SEM
Nanoparticle
Diesel exhaust particle
Atmospheric environment

ABSTRACT

In this study, we attempted to characterize environmental nanoparticles and particle diameter distributions in the atmospheric environment neighboring a traffic route by using a scanning mobility particle sizer (SMPS). The composition of the environmental nanoparticles was analyzed using time-of-flight secondary ion mass spectrometry (TOF-SIMS). It was observed that the environmental nanoparticles showed peaks at 20 nm and 100 nm. The secondary ions C^+, O^+, Si^+, and SiH_3^+ were strongly detected in the environmental nanoparticles with a peak at 20 nm. On the other hand, the secondary ions NH_4^+, Na^+, K^+, and Ca^+ were detected in the environmental nanoparticles with a peak at 100 nm. Moreover, it was found that the secondary ion spectral patterns of the organic compounds were different for each particle diameter. Hence, we concluded that the combination of the SMPS with TOF-SIMS is a powerful technique to characterize environmental nanoparticles.

1. Introduction

Particulate matter (PM) in the atmospheric environment has adverse health effects on humans. [1] In particular, many researchers on environmental toxicology have stated that diesel exhaust particles (DEPs) emitted from a diesel engine have a negative influence on the respiratory system, male reproductive system, and central nervous system. [2–4] Furthermore, Kittelson at Minnesota University reported that the DEP number is mostly in the nanoparticle range. [5] It appears that many diesel exhaust nanoparticles with a diameter less than 100 nm are emitted into the atmospheric environment. However, it has not been possible to obtain detailed information on environmental nanoparticles. Hence, it is very important to investigate nanoparticle properties such as the particle number, particle diameter, and particle composition and the source of nanoparticles.

The environmental quality standard for atmospheric PM with a diameter less than 10 μm (PM_{10}) in Japan specifies that the daily average of hourly values shall not exceed 0.10 mg/m^3 and that the hourly values shall not exceed 0.20 mg/m^3. [6] Recently, an environmental quality standard has been suggested for PM with a size less than 100 nm ($PM_{0.1}$) because it may be considerably toxic. In the Tokyo metropolitan area, a diesel-powered vehicle is required to install a diesel particle filter (DPF) to remove DEPs. [7] Furthermore, Gonzalez-Flecha at the Harvard School of Public Health has shown that harmful developments in the lung and heart that follow particulate air pollution inhalation are associated with the composition of the particulate particles (silicon, iron, aluminum, etc.) [8]; this indicates that obtained information of the compositions were important in the health influences on human body. Thus, from the viewpoint of particulate air pollution, it is desirable to elucidate the relation between nanoparticle properties and health effects resulting from exposure to nanoparticles.

Hence, in this study, we characterized the nanoparticles in the atmospheric environment. The particle diameter distributions of the nanoparticles were determined using a scanning mobility particle sizer (SMPS), while the composition of the nanoparticles was obtained by employing time-of-flight secondary ion mass spectrometry (TOF-SIMS).

2. Experimental

We attempted to investigate the particle diameter distribution of nanoparticles in the atmospheric environment neighboring a traffic route. The SMPS apparatus (model 3936, TSI Inc.) comprised a condensation particle counter (CPC, model 3782) and a differential mobility analyzer (DMA, model 3081). [9] The operating conditions of the SMPS were a sample flow of 0.6 L/min, a sheath flow of 6.0 L/min, and a particle diameter range of 10–410 nm. After gaining knowledge on specific particle diameter distributions, the environmental nanoparticles were separated using the DMA. The separated nanoparticles (particle diameters: 20 nm and 100 nm) were collected on a GaAs wafer and a TEM grid

* Corresponding author.
E-mail address: j7207660@ed.noda.tus.ac.jp (N. Fukuhara).

0169-4332/$ – see front matter © 2008 Elsevier B.V. All rights reserved.
doi:10.1016/j.apsusc.2008.05.013

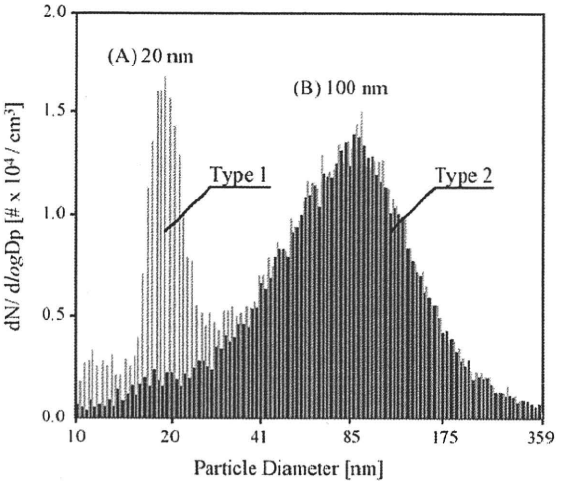

Fig. 1. Particle diameter distributions of nanoparticles in the neighborhood of the traffic route.

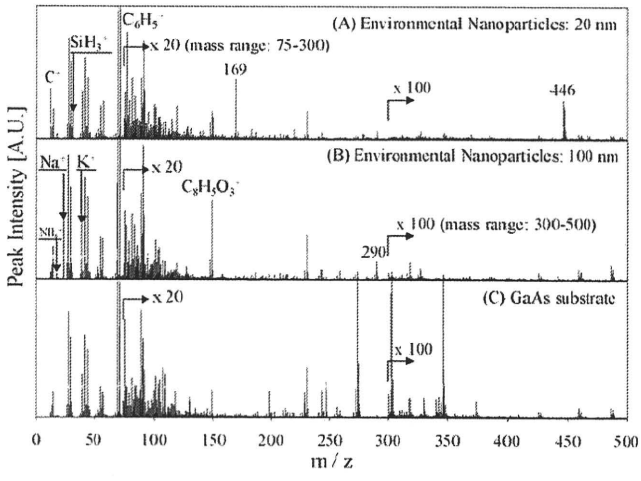

Fig. 3. TOF-SIMS spectra of characteristic environmental nanoparticles (particle diameter: 20 nm or 100 nm).

using an aerosol sampler based on electrostatic force (SSPM, Shimadzu Co.). The SSPM conditions comprised 0.6 L/min of sample flow and 30 min of sampling time. At the sampling location, the mass concentration of the PM was 0.05 mg/m^3 as determined by an aerosol mass monitor (Model 3521, Kanomax Inc.). The traffic frequency was 1758 passes/h for diesel vehicles and 960 passes/h for gasoline vehicles.

We obtained the secondary electron images of the separated environmental nanoparticles using a field-emission-type scanning electron microscope (FE-SEM, JEOL Ltd.) to confirm whether the separation was performed precisely. The detailed composition of the environmental nanoparticles was determined using TOF-SIMS (TRIFT^{TM} 2, ULVAC-PHI Co.).

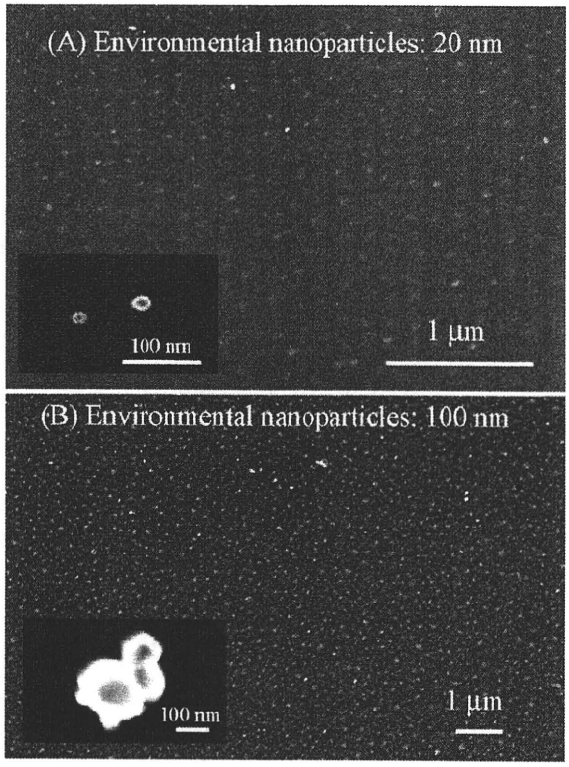

Fig. 2. Secondary electron images of environmental nanoparticles separated using the DMA.

3. Results and discussion

The particle diameter distributions of the nanoparticles in the atmospheric environment neighboring the traffic route are shown in Fig. 1 (Types 1 and 2). From these results, the particle diameter distributions are observed to show peaks at 20 nm and 100 nm (Fig. 1, Type 1). Sometimes, we observed only the 100 nm peak (Fig. 1, Type 2). These particle diameter distributions resemble those of DEPs. Kubo at Toyota Central R&D Laboratory reported that DEPs showed peaks at 20 nm and 100 nm at idling load and a peak at 100 nm at normal load [10]. Hence, there is a possibility of many environmental nanoparticles being generated from diesel vehicles for different engine conditions.

The secondary electron images of the separated environmental nanoparticles are shown in Fig. 2(A and B). From the FE-SEM observations, the separation of the environmental nanoparticles is observed to have been performed precisely. Additionally, it became clear that the environmental nanoparticles with a peak at 20 nm were single spherical nanoparticles (Fig. 2A) and those with a peak at 100 nm comprised both single spherical nanoparticles and aggregated nanoparticles (Fig. 2B). We analyzed each type of separated environmental nanoparticles (20 nm, 100 nm) by TOF-SIMS. The TOF-SIMS spectra and the spectral intensities obtained from the environmental nanoparticles are shown in Fig. 3 and Table 1 (A: 20 nm, B: 100 nm). From the results of TOF-SIMS analyses, the secondary ions C^+, O^+, Si^+, and SiH_3^+ were

Table 1
The spectral intensities of TOF-SIMS spectra from characteristic environmental nanoparticles (particle diameter : 20 nm or 100 nm)

m/z	Secondary ion	Spectral intensity [×10^4 counts]		
		(A) 20 nm	(B) 100 nm	(C) Substrate
12.000	C^+	**31 (0.18)**	3.5 (0.54)	1.7 (0.76)
15.995	O^+	**0.34 (1.7)**	0.044 (4.8)	0.014 (8.4)
27.977	Si^+	**5.9 (0.41)**	5.7 (0.42)	0.68 (1.2)
31.000	SiH_3^+	**10 (0.31)**	0.59 (1.3)	0.14 (2.6)
77.039	$C_6H_5^+$	**2.8 (0.59)**	1.5 (0.82)	0.94 (1.0)
168.989	–	**3.1 (0.57)**	0.19 (2.3)	0.084 (3.5)
445.912	–	**0.34 (1.7)**	0.0048 (14)	–
18.034	NH_4^+	1.5 (0.82)	**1.9 (0.73)**	0.48 (8.4)
22.990	Na^+	0.70 (1.2)	**23 (0.21)**	0.036 (5.3)
38.964	K^+	0.36 (1.7)	**5.6 (0.42)**	0.078 (3.6)
39.963	Ca+	0.015 (8.3)	**0.68 (1.2)**	0.33 (1.7)

Significance of bold values shows the intensity detected strong than other type of particles.

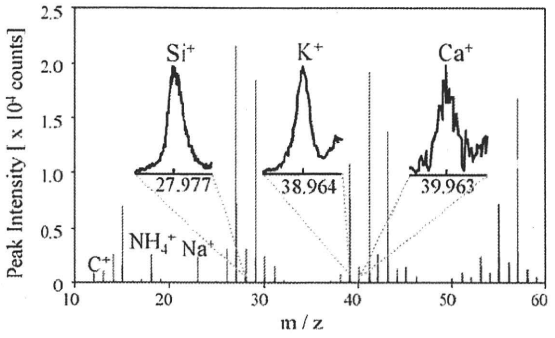

Fig. 4. TOF-SIMS spectrum of DEPs collected from a diesel vehicle.

observed to be strongly detected in the environmental nanoparticles with a peak at 20 nm (Fig. 3A). On the other hand, the secondary ions NH_4^+, Na^+, K^+, and Ca^+ were strongly detected in the environmental nanoparticles with a peak at 100 nm (Fig. 3B). Furthermore, it became clear that secondary ion spectra such as those of $C_6H_5^+$, $C_8H_5O_3^+$, 169, 290, and 446 were different for different particle diameters (20 nm or 100 nm). These secondary ion intensities obtained from the environmental nanoparticles were higher than those of the background spectrum (Fig. 3C). Thus, we could obtain the detailed composition of the environmental nanoparticles.

It appears that the environmental nanoparticles with a peak at 20 nm comprise organic compounds such as fuels and engine oils. Some elements detected from the environmental nanoparticles with a peak at 100 nm were similar to those in DEPs. The TOF-SIMS spectrum and characteristic secondary ions of DEPs are shown in Fig. 4. The secondary ions NH_4^+, Na^+, Si^+, K^+, and Ca^+ were clearly detected in the DEPs. Thus, the composition of the environmental nanoparticles with a peak at 100 nm corresponded well to the obtained compositional information of DEPs. We concluded that the environmental nanoparticles with a peak at 100 nm were DEPs.

4. Conclusion

In this study, we investigated nanoparticles in the atmospheric environment neighboring a traffic route by using an SMPS, an FE-SEM, and TOF-SIMS. From both SMPS measurements and FE-SEM observations, the environmental nanoparticles were observed to show peaks at 20 nm and 100 nm. From the TOF-SIMS analyses, it was found that the secondary ion spectra were different for different types (20 nm and 100 nm) of environmental nanoparticles. Moreover, the obtained compositional information for the environmental nanoparticles with a peak at 100 nm corresponded well to the DEP composition. Therefore, we concluded that the combination of the SMPS with TOF-SIMS is a powerful technique to characterize environmental nanoparticles.

Acknowledgements

We gratefully acknowledge Mitsubishi Gas Chemical Co. Inc. for its cooperation in the TOF-SIMS analysis and Tokyo Dylec Co. for support with the SMPS measurements. We thank Mr. S. Nakamura at the Science University of Tokyo and Dr. B. Tomiyasu at the University of Tokyo for their kind support and fruitful discussions.

References

[1] D.W. Dockery, C.A. Pope, X. Xu, J.D. Spengler, J.H. Ware, M.E. Fay, B.G. Ferris, F.E. Speizer, New Eng. J. Med. 329 (1993) 1753–1759.
[2] T. Ichinose, Y. Yajima, M. Nagashima, S. Takenoshita, Y. Nagamachi, M. Sugai, Carcinogenesis 18 (1997) 185–192.
[3] S. Yoshida, M. Sagai, S. Oshio, T. Umeda, T. Ihara, M. Sugamata, I. Sugawara, K. Takeda, Int. J. Androl. 22 (5) (1999) 307–315.
[4] M. Sugamata, T. Ihara, H. Takano, S. Oshio, K. Takeda, J. Health Sci. 52 (1) (2006) 82–84.
[5] D.B. Kittelson, J. Aerosol. Sci. 295–6 (1998) 575–588.
[6] Ministry of Environment, http://www.env.go.jp/en/air/aq/aq.html.
[7] Tokyo Metropolitan Government, http://www.metro.tokyo.jp/ENGLISH/index.html.
[8] S.A. Gurgueira, J. Lawrence, B. Coull, G.G.K. Murthy, B. González-Flecha, Environ. Health Perspect. 110 (2002) 749–755.
[9] Tokyo Dylec Co., http://www.t-dylec.net/index.html.
[10] T. Yoshida. NTS Inc., Tokyo 2005, 40–41.

Colloid Polym Sci
DOI 10.1007/s00396-010-2317-4

SHORT COMMUNICATION

Dependence of the dispersion behavior of [60]fullerene in aqueous media on the chain length of poly (*N*-isopropylacrylamide) as a dispersing agent

Katsumi Uchida · Atsushi Tamura · Naoyuki Fukushima · Hirofumi Yajima

Received: 8 July 2010 / Revised: 31 August 2010 / Accepted: 18 September 2010

Abstract We have investigated the effect of the chain length of temperature-sensitive poly(*N*-isopropylacrylamide) (PIPAAm) on the dispersion of [60]fullerene (C_{60}) in aqueous media through an interaction between PIPAAm and C_{60} below the lower critical solution temperature (LCST) of PIPAAm. UV–vis absorption spectral measurements showed that the saturated amount of the dispersed C_{60} increased in proportion to the chain length of the PIPAAm. Additionally, an absorption band at around 430 nm was observed in the dispersed C_{60} solution and was assigned to a C_{60}/PIPAAm complex. The complex formed an amorphous molecular assembly between C_{60} molecules and PIPAAm chains, the structure of which was confirmed in a transmission electron microscopy image. Dynamic light scattering measurements indicated that the particle size of the C_{60}/PIPAAm complex increased with the chain length of the PIPAAm. From electrophoretic laser light scattering measurements, the zeta potential of the C_{60}/PIPAAm complex was found to be shifted from a negative value to zero with an increase in the chain length of PIPAAm. Longer PIPAAm chains, however, gave rise to a higher dispersion stability of the complex. Similar to the dispersion behavior of PIPAAm-C_{60} conjugates in aqueous solutions, the aqueous C_{60} dispersion with PIPAAm exhibited rapid, and reversible dispersion–aggregation changes in response to temperature alternation across the LCST.

Keywords [60]Fullerene · Poly(*N*-isopropylacrylamide) · Complex · Dispersion · Reversibility

Introduction

Fullerene C_{60}, because of its unique biological activities including enzyme inhibition [1], photo-induced activated-oxygen generation [1, 2], and antioxidant behavior [3], has attracted much attention with regard to its potential application as a bio-nanomaterial. The insolubility of C_{60} in water, however, has significantly hampered many of its practical uses. This drawback has been overcome by chemical modification of C_{60} with hydrophilic functional groups [1] or hydrophilic polymer chains [4], complexation of C_{60} and hydrophilic polymer chains [5], and a solvent exchange technique that involves mixing pre-dissolved fullerene in an organic solvent such as tetrahydofuran (THF) with water [6]. In particular, the introduction of water-soluble polymers to C_{60} has been recognized as one of the simplest strategies to enhance its solubility in water, while retaining the unique properties of C_{60} [7]. In recent years, considerable research attention has been focused on not only the solubilization of C_{60} in water or polar solvents but also the interesting morphologies and unique self-assembly behaviors of stimuli-responsive C_{60} polymeric systems [8–14]. For example, C_{60}-containing poly[2-(dimethylamino)-ethyl methacrylate] (C_{60}-*b*-PDMAEMA) synthesized by atom transfer radical polymerization (ATRP) exhibited temperature- and pH-responsive solution behaviors in water [10]. Micellar

Electronic supplementary material The online version of this article (doi:10.1007/s00396-010-2317-4) contains supplementary material, which is available to authorized users.

K. Uchida · A. Tamura · N. Fukushima · H. Yajima (✉)
Department of Applied Chemistry,
Tokyo University of Science,
1-3 Kagurazaka, Shinjuku-ku,
Tokyo 162-8601, Japan
e-mail: yajima@rs.kagu.tus.ac.jp

K. Uchida
e-mail: kauchida@rs.kagu.tus.ac.jp

Published online: 31 October 2010

aggregates coexisted with unimeric C_{60}-*b*-PDMAEMA at low pHs and all temperatures. At high pHs, insoluble C_{60}-*b*-PDMAEMA suspensions were produced at high temperatures and they transform into unimeric C_{60}-*b*-PDMAEMA particles at temperatures below the lower critical solution temperature (LCST) of PDMAEMA. Liu and co-workers reported that amphiphilic polystyrene-C_{60}-poly(*N*-isopropylacrylamide) (PSt-C_{60}-PIPAAm) block copolymer prepared through ATRP self-assembled into toroidal nanostructures in chloroform [14]. For use of the bioactivity of stimuli-responsive C_{60} polymeric systems, it is necessary to scrutinize the relation between their bioactivity and structure properties such as self-assembly behaviors in solvent.

PIPAAm is a representative temperature-responsive polymer that exhibits a reversible temperature-dependent soluble/insoluble transition at its LCST in water [15]. By exploiting the thermoresponsive conformational changes of PIPAAm, PIPAAm-based materials were produced for controlled drug delivery [16], molecular separation [17], and tissue culture substrates [18], since the LCST of PIPAAm in water is close to body temperature. For example, the PIPAAm's phase transition induced to the structural deformations of the inner core in the polymeric micelle comprised of PIPAAm-*b*-poly(butyl methacrylate) (PIPAAm-*b*-PBMA), resulting in controlled release of drug loaded in the core. Among external stimuli, high temperature, namely, heat, is one of the best signals in terms of easy and safe medical applications. Moreover, hyperthermia treatment has been shown to synergistically enhance tumor cytotoxicity when combined with chemo- or radio-therapy in clinical studies [19, 20]. Therefore, in order to develop a functionalized C_{60} derivative possessing heat-induced accumulation and bioactivity for use in photodynamic tumor therapy and thermotherapy, we have synthesized thermoresponsive conjugates of C_{60} and PIPAAm (PIPAAm-C_{60}) with different chain lengths by ATRP and investigated their temperature-responsive phase transition behavior [9]. Depending on the chain length, the coexistence of unimers (size of ca. 5–10 nm) and molecular assemblies (size of ca. 85 nm) of PIPAAm-C_{60} was observed below the lower critical solution temperature of PIPAAm by gel permeation chromatography and dynamic light scattering studies, demonstrating that PIPAAm-C_{60} exhibited a two-step thermoresponsive phase transition caused by the unimers and molecular assemblies, respectively.

Interestingly, below the LCST, longer PIPAAm chains induced formation of an increasing amount of unimers. From this finding, it is inferred that, due to the presence of carbonyl groups in PIPAAm, PIPAAm interacts with C_{60} in a manner analogous to poly(vinylpyrrolidone) (PVP). Due to the existence of the unimers, PIPAAm would be expected to play an intrinsic role as a dispersant for C_{60} analogous to PVP, which also possesses carbonyl groups and can disperse C_{60} in water through a charge transfer interaction between C_{60} as an electron acceptor and PVP as an electron donor [21]. Hence, the objective of this paper is to investigate the temperature-responsive dispersion behavior of C_{60} in water through an interaction with PIPAAm, and to probe the effects of the molecular weight of PIPAAm on the physicochemical properties of C_{60}/PIPAAm complexes.

Materials and methods

Materials

Fullerene C_{60} (99.99%) was purchased from Materials Technologies Research Ltd. (Cleveland, OH, USA) and used as received. *N*-Isopropylacrylamide (IPAAm) was kindly provided by KOHJIN (Tokyo, Japan) and was purified by recrystallization from hexane and dried at 25 °C in vacuo. Tris[(2-dimethylamino)ethyl]amine (Me_6TREN) was synthesized according to the published procedure [22]. Methyl 2-chloropropionate (MCP; 97%) was obtained from Tokyo Kasei Kogyo Co., Ltd. (Tokyo, Japan) and distilled under reduced pressure. Copper (I) chloride (CuCl; 99.995%) was purchased from Sigma-Aldrich (Milwaukee, WI, USA) and was used as received. All solvents were purchased from Kanto Kagaku Co., Ltd., (Tokyo, Japan).

Synthesis of PIPAAm by atom transfer radical polymerization

Four series of well-defined PIPAAms with different molecular weights were synthesized by the ATRP technique using IPAAm as a monomer, CuCl/Me_6TREN as a catalyst and MCP as an initiator [9, 23, 24]. The molecular weight of the PIPAAms, denoted PIPAAm2k, PIPAAm6k, PIPAAm20k, and PIPAAm48k, were 2,250, 6,000, 20,380, and 48,400, respectively. Their characterization data are summarized in Table 1.

Dispersion of C_{60} by PIPAAm as a dispersing agent

According to the method reported by Yamakoshi et al. [5], C_{60} was dispersed in aqueous solutions by using synthesized PIPAAm. Briefly, 50 mg PIPAAm was dissolved in 4.0 mL chloroform and pristine 1.8 mg C_{60} was sufficiently dissolved in 1.0 mL toluene by stirring, respectively. Both solutions were mixed together and stirred for 1 h. The mixture was then completely evaporated under reduced pressure, and the residue was dispersed in 4.5 mL ultra-pure water by ultrasonication. The undispersed residue was filtered off with a 0.45-μm polytetrafluoroethylene filter. The final volume of the ultra-pure water was adjusted to 5.0 mL.

Table 1 Characteristics of PIPAAm and saturated C_{60} solubility in aqueous media

Code	M_n (Da)[a]	M_w/M_n[b]	LCST (°C)[c]	C_{60} solubility (μg/mL)[d]
PIPAAm2k	2,250	1.21	43.7	2.4±0.4
PIPAAm6k	6,000	1.14	36.1	8.0±2.4
PIPAAm20k	20,380	1.13	35.1	18.6±5.3
PIPAAm48k	48,400	1.14	34.1	48.4±5.4

[a] Determined from ^{1}H nuclear magnetic resonance spectra

[b] Determined by gel permeation chromatography in tetrahydrofuran

[c] Determined by turbidimetry. The LCST of PIPAAm itself is nearly identical to that for the C_{60}/PIPAAm complex, regardless of the molecular weight of PIPAAm

[d] n=4±standard deviation (SD); the polymer concentration was 10.0 mg/mL

Measurements

By ^{1}H nuclear magnetic resonance spectrometry (500 MHz, JNM-LA500, JEOL, Tokyo, Japan) using D_2O (Kanto Chemical, Tokyo, Japan), number-averaged molecular weights (M_n) of the synthesized PIPAAms were estimated from the ratio of the integral areas of the terminal methoxy protons (3.7 ppm) to that of the methine protons (3.9 ppm) of the polymer side chain. Additionally, polydispersity indices (PIDs; M_w/M_n) of the PIPAAms were determined by gel permeation chromatography (CCP-8020, Tosoh, Tokyo, Japan) with an RI (refractive index) detector system (RI-8022, Tosoh) using THF as the mobile phase (at a flow rate of 1.0 mL/min at 40 °C). This data is also summarized in Table 1.

The absorption spectra of aqueous solutions of C_{60} dispersed by PIPAAms were observed with an ultraviolet–visible-near-infrared spectrometer (V-570, Jasco, Tokyo, Japan) at 20.0 °C. Optical transmittance of the aqueous solutions of the C_{60}/PIPAAm complexes were measured at 600 nm with the V-570 equipped with a ETC-505T peltier-type thermostatic cell holder (Jasco, Tokyo, Japan) at a heating or cooling rate of 0.5 °C/min in the temperature range from 20 °C to 40 °C. The LCST was defined as the temperature at which the initial transmission at 20 °C was reduced by 50%.

Dynamic light scattering (DLS) measurements of the C_{60}/PIPAAm complexes were carried out on a DLS-7000 instrument (Otsuka Electronics Co., Ltd., Osaka, Japan) equipped with an argon ion (Ar^+) laser at a wavelength of 488 nm, a scattering angle of 90° and a temperature of 20.0 °C. From the time correlation function of the scattering intensity, the decay time distribution function was obtained with an inverse Laplace transform program (CONTIN) provided by ALV (Langen, Germany), where the hydrodynamic radius (R_h) of the C_{60}/PIPAAm complex was determined from the Stokes–Einstein equation [25].

By electrophoretic laser light scattering (ELS) measurements at 20.0 °C (ELS-Z1 system, Otsuka Electronics Co., Ltd., Osaka, Japan), the zeta potential of the C_{60}/PIPAAm complex was analyzed according to the Smoluchowski equation [26]. .

Transmission electron microscope (TEM) images of the dispersed C_{60}/PIPAAm complexes were observed with an H-9500 (Hitachi Co., Ltd., Tokyo, Japan).

Results and discussion

A representative UV–vis absorption spectrum for an aqueous solution of C_{60} dispersed by PIPAAm (PIPAAm48k) is shown in Fig. 1. Notably, similar spectral patterns were observed regardless of the molecular weight of PIPAAm. Compared to the absorption spectrum of pristine C_{60} dispersed in hexane, a novel absorption band was observed at around 430 nm. A similar band is observed in the aqueous solution of C_{60} dispersed by PVP, which is assigned to a C_{60}/PVP charge-transfer complex [5, 21]. It is thus inferred from these results that, due to the presence of the carbonyl group in PIPAAm, PIPAAm interacts similarly with C_{60}. The novel band in the UV–vis spectrum is therefore assigned to a C_{60}/PIPAAm complex. Interestingly,

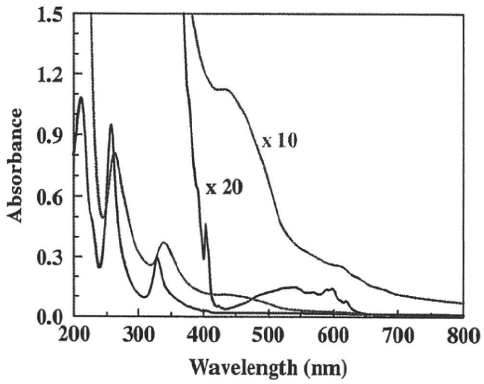

Fig. 1 UV-visible absorption spectra of the C_{60}/PIPAAm48k complex in aqueous media (*blue line*) and pristine C_{60} in hexane (*black line*) at 20.0 °C. *Inserts* are the same spectra at the magnifications indicated

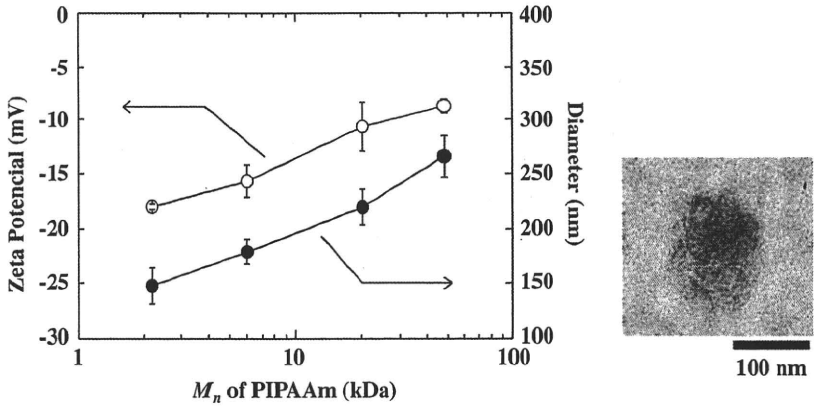

Fig. 2 Changes in the diameter (*closed circle*) and zeta potential (*open circle*) of the C_{60}/PIPAAm complex in aqueous media at 20.0 °C as a function of the M_n of PIPAAm (n=4, ±SD). The *inset* shows a TEM image of a C_{60}/PIPAAm2k complex. *Scale bar* is 100 nm

the conjugates [9] of PIPAAm and C_{60} synthesized by the atom transfer radical polymerization technique possessed a similar band at around 430 nm. Differences in PIPAAm chain length, however, gave rise to differences in this band (see Figure S1 in Supporting Information) [27]. This finding indicates that the interaction between PIPAAm and C_{60} in the conjugates is dependent on the molecular weight of the PIPAAm and thus is a key factor for controlling the dispersion state of the conjugate.

The specific absorption band of C_{60} at around 330 nm was also observed in the spectra of aqueous solutions of C_{60} dispersed by PIPAAms. The amount of C_{60} dispersed by each PIPAAm was estimated using the molar absorption coefficient of C_{60} at 340 nm (ε_{340}=49,000) cited in the case of PVP [5]. Conforming to the dispersion properties of C_{60} in the C_{60}/PVP complex system [5], the saturated amount of C_{60} dispersed by PIPAAm increased linearly in proportion to the amount of PIPAAm. For the C_{60}/PIPAAm48k complex system, the saturated amount of the dispersed C_{60}

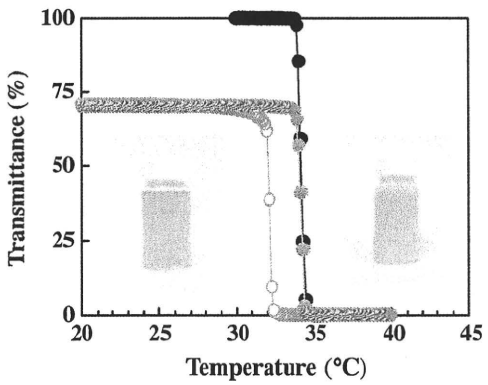

Fig. 3 Temperature dependence of the optical transmittance at 600 nm of the C_{60}/PIPAAm48k complex in aqueous media at a heating (*orange line including closed circle*)/cooling (*orange line including open circle*) rate of 0.5 °C/min in the temperature range from 20 °C to 40 °C. As a control, transmittance changes for PIPAAm48k itself upon heating are shown (*black line*). The *inset* photographs show aqueous solutions of the C_{60}/PIPAAm48k complex (*left* at 20 °C, *right* at 40 °C)

in water was 48.4 μg/mL at a polymer concentration of 10 mg/mL. Additionally, at a polymer concentration of 10 mg/mL, the saturated amount of dispersed C_{60} increased with increasing molecular weight of the PIPAAm dispersing agent, as shown in Table 1. This finding implies that the higher the molecular weight of PIPAAm, the stronger the interaction between C_{60} and PIPAAm due to multiple-point interactions. Indeed, the C_{60}/PIPAAm2k complex was aggregated for only a few weeks, while the aqueous dispersion of the C_{60}/PIPAAm48k complex was highly stable and showed no precipitation after storage for 5 months at room temperature. These results indicate that not only the saturated amount of the dispersed C_{60} but also the dispersion stability of the complex is dependent on the molecular weight of PIPAAm.

The particle diameter and zeta potential of the C_{60}/PIPAAm complexes were determined as a function of the molecular weight of PIPAAm at 20 °C (below the LCST), as shown in Fig. 2. As determined by DLS measurements and similar to the C_{60}/PVP complex [28, 29], the C_{60}/PIPAAm complex formed a nanoparticle structure with a relatively narrow size distribution (μ_2/Γ^2=~0.1) in aqueous media, regardless of the molecular weight of PIPAAm. Moreover, the TEM image of the C_{60}/PIPAAm2k complex in the inset in Fig. 2 shows that the C_{60}/PIPAAm complex forms an amorphous molecular assembly between the C_{60} molecules and PIPAAm chains [30]. The particle size of the C_{60}/PIPAAm complex increased in proportion to the molecular weight of PIPAAm. By using longer PIPAAm chains, the amount of C_{60} moieties interacting with PIPAAm increased, resulting in an increase in the association number of PIPAAm and C_{60}, and thus an increase of the particle size of the complex. Interestingly, the C_{60}/PIPAAm complex with a larger particle size possessed a higher dispersion stability in water. It is inferred that the high stability of the complex is induced by steric repulsion of the longer PIPAAm chains.

This conclusion was supported by ELS measurements. The zeta potential of the C_{60}/PIPAAm2k complex was

negatively charged, while the zeta potential of the C_{60}/PIPAAm complex was shifted from a negative to a neutral value with an increase in the chain length of PIPAAm. It has been hypothesized that C_{60} acquires a charge through charge transfer from the oxygen atoms of water and hydroxylation of its surface through either adsorption of hydroxyl groups or hydrolysis [6]. Assuming this hypothesis to be correct, the negative zeta potential value of the complex is thought to be caused by the C_{60} moieties. This trend in the zeta potential is attributed to the shielding effect induced by the adsorption of the longer polymer chains to C_{60}. In general, colloidal particles are dispersed in water by the electrostatic repulsion between the positively or negatively charged colloids. Thus, the shift of the colloidal zeta potential to neutral induces a reduction of the dispersion stability of the colloid. In spite of neutralization, however, the C_{60}/PIPAAm complex was highly dispersed in water. It is thus inferred that the high dispersion stabilization of the C_{60}/PIPAAm complex by longer PIPAAm chains in aqueous media is induced not by electrostatic repulsion between the complexes but by steric repulsion of the adsorbed PIPAAm chains.

Analogous to PIPAAm itself [23], the LCST of the C_{60}/PIPAAm complexes shifted to lower temperatures with increasing PIPAAm chain length (Table 1). In fact, the LCSTs of the C_{60}/PIPAAm complexes are nearly identical to PIPAAm itself, regardless of the molecular weight of PIPAAm (data not shown). Transmittance changes for a typical C_{60}/PIPAAm48k complex aqueous solution in response to reversible temperature changes across the LCST are shown in Fig. 3. At 20 °C (below the LCST), the transmittance of the aqueous solution of the C_{60}/PIPAAm48k complex was about 70%. The solution rapidly became turbid at around 34 °C and the transmittance changed according to a one-step behavior profile similar to free PIPAAm chains. It should be noted that free PIPAAm chains that do not interact with C_{60} exist in substantial amounts in the C_{60}/PIPAAm complex system. Thus, owing to the high ratio of PPAAm to C_{60}, the influence of C_{60} on the LCST of PIPAAm is negligible. After cooling the heated complex solution, the transmittance was restored and remained unchanged at about 70%. At 20 °C, the C_{60}/PIPAAm48k complex was highly dispersed in water in spite of reversible temperature changes across the LCST, which was confirmed by DLS measurements (data not shown). Above the LCST, the transmittance of the C_{60}/PIPAAm48k complex solution was reduced almost to zero and was accompanied by aggregation of the C_{60}/PIPAAm48k complexes. The transmittance profile in response to reversible temperature changes exhibited hysteresis. This result indicates that in spite of the lack of covalent bonding between C_{60} and PIPAAm, the C_{60}/PIPAAm complexes undergo temperature-responsive reversible dispersion–aggregation changes.

Conclusion

In summary, the effect of PIPAAm chain length on the performance of PIPAAm as a dispersing agent for C_{60} in water was investigated. While there is no covalent bonding between C_{60} and PIPAAm, the dispersed C_{60} formed a complex with PIPAAm due to interactions between C_{60} and PIPAAm. These interactions were dependent on the chain length of PIPAAm. Longer PIPAAm chains led to an increase in the amount of dispersed C_{60} and the stability and particle size of the C_{60}/PIPAAm complex. The C_{60}/PIPAAm complex exhibited temperature-responsive reversible dispersion–aggregation changes. The chain length of PIPAAm was found to be the predominant factor involved in the dispersion properties and solution characteristics of the C_{60} dispersed by PIPAAm, with or without covalent bonding between C_{60} and PIPAAm in the complex. Dispersion of C_{60} in aqueous media using this type of environmental stimulus-sensitive polymer under moderate conditions is a simple and convenient method and is potentially applicable for development of an intelligent biomaterial exhibiting bioactivities and capable of heat-induced accumulation.

Acknowledgments This work was supported in part by a Grant-in-Aid from the Health Sciences of Nanoparticles of the Tokyo University of Science. The authors are thankful to Mr. Yosuke Kaji and Ms. Yu Echigo of the Tokyo University of Science for their valuable comments with respect to the C_{60} dispersion.

References

1. Nakamura E, Isobe H (2003) Acc Chem Res 36:807–815
2. Yamakoshi Y, Sueyoshi S, Fukuhara K, Miyata N, Masumizu T, Kohno M (1998) J Am Chem Soc 120:12363–12364
3. Gharbi N, Pressac M, Hadchouel M, Szwarc H, Wilson SR, Moussa F (2005) Nano Lett 5:2578–2585
4. Song T, Dai S, Tam KC, Lee SY, Goh SH (2003) Langmuir 19:4798–4803
5. Yamakoshi YN, Yagami T, Fukuhara K, Sueyoshi S, Miyata N (1994) J Chem Soc Chem Commun 517–518
6. Deguchi S, Alargova RG, Tsujii K (2001) Langmuir 17:6013–6017
7. Vitakini D, Spina E, Dattilo S, Mineo P, Scamporrino E (2008) J Polym Sci A Polym Chem 46:2145–2153
8. Tamura A, Uchida K, Yajima H (2006) Chem Lett 35:282–283
9. Uchida K, Tamura A, Yajima H (2010) Biointerphases 5:17–21
10. Dai S, Ravi P, Tan CH, Tam KC (2004) Langmuir 20:8569–8575
11. Ravi P, Wang C, Dai S, Tam KC (2006) Langmuir 22:7167–7174
12. Zhou G, Harruna II, Zhou WL, Aicher WK, Geckeler KE (2007) Chem Eur J 13:569–573
13. Li C, Hu J, Yin J, Liu S (2009) Macromol 42:5007–5016
14. Liu YL, Chang YH, Chen WH (2008) Macromol 41:7857–7862
15. Heskins M, Guillet JE (1968) Macromol Sci Chem A2:1441–1455
16. Chung JE, Yokoyama M, Okano T (2000) J Contol Release 65:93–103
17. Kikuchi A, Okano T (2002) Prog Polym Sci 27:1165–1193

18. Yamada N, Okano T, Sakai H, Karikusa F, Sawasaki Y, Sakurai Y (1990) Macromol Chem Rapid Commun 11:571–576
19. Liu W, Dreher MR, Furgeson DY, Peixoto KV, Yuan H, Zalutsky MR, Chilkoti (2006) J Control Release 116:170–178
20. Kinuya S, Yokoyama K, Michigishi T, Tonami N (2004) Int J Hypertherm 20:190–200
21. Ungurenasu C, Airinei A (2000) J Med Chem 43:3186–3188
22. Queffelec J, Gaynor SG, Matyjaszewski K (2000) Macromol 33:8629–8639
23. Xia Y, Yin X, Bruke NAD, Stöver HDH (2005) Macromol 38:5937–5943
24. Xia Y, Bruke NAD, Stöver HDH (2006) Macromol 39:2275–2283
25. Wang X, Goh SH, Lu ZH, Lee SY, Wu C (1999) Macromol 32:2786–2788
26. Brant JA, Labille J, Bottero J, Wiesner MR (2006) Langmuir 22:3878–3885
27. Supporting Information: UV-vis absorption spectra for conjugates of PIPAAm and C_{60}
28. Sushko ML, Tenhu H, Klenin SI (2002) Polymer 43:2769–2775
29. Xiao L, Takada H, Gana XH, Miwa N (2006) Bioorg Med Chem Lett 16:1590–1595
30. Laiho A, Ras RHA, Valkama S, Ruokolainen J, Österbacka R, Ikkala O (2006) Macomol 39:7648–7653

Effect of the polymer chain length of poly(*N*-isopropylacrylamide) on the temperature-responsive phase transition behavior of its conjugates with [60]fullerene

Katsumi Uchida, Atsushi Tamura, and Hirofumi Yajima[a)]
Department of Applied Chemistry, Tokyo University of Science, 12-1 Funagawara-cho, Ichigaya, Shinjuku-ku, Tokyo 162-0826, Japan

(Received 10 December 2009; accepted 15 January 2010; published 29 March 2010)

In order to develop biomedical materials with specific functionalities, thermoresponsive conjugates [poly(*N*-isopropylacrylamide)-C_{60} (PIPAAm-C_{60})]of [60]fullerene (C_{60}) and PIPAAm with two different polymer chain lengths (4 and 20 kDa) were synthesized by atom transfer radical polymerization. The effects of the polymer chain length on the temperature-responsive phase transition behavior of the synthetic PIPAAm-C_{60} conjugates were probed by means of various physicochemical techniques. The coexistence of unimers and molecular assemblies of PIPAAm-C_{60} was observed by gel permeation chromatography and dynamic light scattering studies in two PIPAAm-C_{60} aqueous solutions below their lower critical solution temperatures (LCSTs). Additionally, below their LCSTs, differences in PIPAAm chain length gave rise to changes in the composition of the unimers and molecular assemblies. In response to temperature, the absorbance of the PIPAAm-C_{60} aqueous solution changed according to a two-step behavior profile. Increasing temperature during the primary stage, where a change in the absorbance of the PIPAAm-C_{60} aqueous solution took place, did not change the transition temperature, regardless of the solution concentration of PIPAAm-C_{60}. This absorbance change was associated with the phase transition of the molecular assemblies of PIPAAm-C_{60}. However, at the second stage, the transition temperature shifted to a higher value with the decrease in the concentration of PIPAAm-C_{60}, in the same manner as free PIPAAm chains. The second change was associated with the phase transition of the unimeric PIPAAm-C_{60}. Differences in PIPAAm chain length gave rise to the change in the phase transition behavior of PIPAAm-C_{60} aqueous solution. Therefore, the chain length of PIPAAm was found to be a predominant factor involved in the solution characteristics of PIPAAm-C_{60}. Consequently, the PIPAAm-C_{60} is expected to be an intelligent biomaterial possessing heat-induced accumulation and bioactivities. © *2010 American Vacuum Society.* [DOI: 10.1116/1.3319348]

I. INTRODUCTION

Fullerene, C_{60}, has recently attracted significant attention because of its unique biological properties, such as antioxidant activity, neuroprotective properties, enzyme inhibition, DNA cleavage, and anticancer activity.[1–6] However, the insolubility of C_{60} in water has hampered many of its biomedical applications, such as photodynamic tumor therapy. One of the strategies to improve its solubility is the chemical modification of C_{60} with hydrophilic compounds, such as alcohols, carboxylic acids, amines, or long-chain hydrophilic polymers.[7–10] To address this issue, we have recently prepared the monoadduct of C_{60} with temperature-responsive poly(*N*-isopropylacrylamide) (PIPAAm) synthesized by means of radical polymerization, and investigated the physicochemical properties of the conjugate (PIPAAm-C_{60}) in water.[11] We have found that PIPAAm-C_{60} exhibits a rapid and reversible temperature-dependent soluble/insoluble transition in response to a narrow range of temperature variation across the lower critical solution temperature (LCST) of the PIPAAm-C_{60}, induced by the phase transition of the PIPAAm chain binding to C_{60}. Turbidity and dynamic light scattering (DLS) measurements implied that below the LCST, the PIPAAm-C_{60} formed a micellelike structure composed of C_{60} molecules as the inner core, whereas above the LCST, the micelles aggregated and the solution turned cloudy. PIPAAm itself is hydrated and expanded in water below its LCST, and changes to a compact form above its LCST by sudden dehydration and inter- and intramolecular hydrophobic interactions.[12–14] The LCST of PIPAAm itself is strongly dependent on its chain length[15] and end groups.[16] PIPAAm with a longer chain or a more hydrophobic end group possesses a lower LCST. In agreement with this, Nakayama and Okano[17] reported that the phase transition of the polymeric micelle comprised of PIPAAm and a hydrophobic polymer was dependent on both the outermost end group of the micelle and the chain length of PIPAAm. Additionally, Chung *et al.*[18] reported that the structural deformations of the micelle's inner core induced by PIPAAm's phase transition were dependent on the hydrophobic component of the inner core.

In order to develop more effective functionalities of PIPAAm-C_{60} as a biomaterial possessing heat-induced accumulation and bioactivities, it is important to probe the effects of the chain length of PIPAAm on the dispersion behavior

a)Author to whom correspondence should be addressed; electronic mail: yajima@rs.kagu.tus.ac.jp

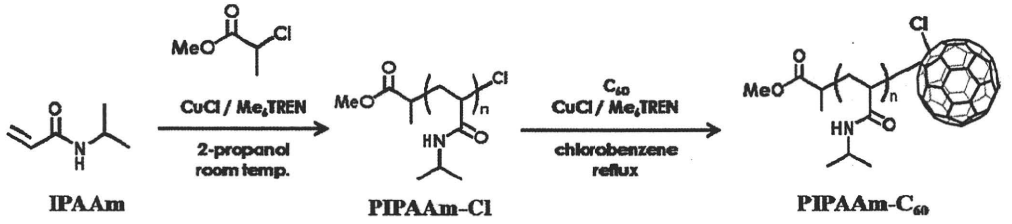

FIG. 1. Reaction scheme for synthesis of PIPAAm-C_{60} by an ATRP technique.

and phase transition of PIPAAm-C_{60} in aqueous solution, in response to temperature. In this study, to eliminate the influence of the polydispersity of PIPAAm to the thermoresponsive solution characteristics of PIPAAm-C_{60}, we have prepared the PIPAAm-C_{60} using the narrow-polydisperse PIPAAm made by atom transfer radical polymerization (ATRP). Then, we have analyzed clearly the thermally sensitive properties of PIPAAm-C_{60} in aqueous solution by turbidity and DLS measurements.

II. EXPERIMENT

A. Materials

C_{60} (99.99%) was obtained from Materials Technologies Research Ltd. (Cleveland, OH, USA). *N*-Isopropylacrylamide (IPAAm) was kindly provided by KOHJIN (Tokyo, Japan) and was purified by recrystallization from hexane and dried at 25 °C *in vacuo*. Tris[(2-dimethylamino)ethyl]amine (Me_6TREN) was prepared according to the method of Queffelec *et al.*[19] Copper (I) chloride (CuCl, 99.995%) and methyl 2-chloropropionate (MCP) (97%) were purchased from Sigma-Aldrich. Chlorobenzene and 2-propanol were obtained from Kanto Chemical Co. (Tokyo, Japan).

B. Preparation of PIPAAm macroinitiator

Well-defined PIPAAm was synthesized by the ATRP technique using CuCl/Me_6TREN as a catalyst (Fig. 1).[15,16] The reactions were carried out at room temperature under argon atmosphere. IPAAm, CuCl and 2-propanol were combined in a Schlenk tube, which was deoxygenated with argon. Me_6TREN was then added and the solution was stirred to allow the formation of the CuCl/Me_6TREN complex. MCP was then added as the initiator. To remove the catalyst and unreacted monomer, the reaction mixture was passed through a neutral alumina column and then the PIPAAm was precipitated in diethyl ether and dried *in vacuo*. The synthesized PIPAAm possessed a chloro group at one end, and hereafter is denoted as PIPAAm-Cl. In this study, two lots of PIPAAm-Cl with different molecular weights were synthesized. The two synthetic PIPAAm-Cls were denoted as P-4 and P-20, and their properties are summarized in Table I.

C. Preparation of PIPAAm-C_{60}

PIPAAm-Cl was used as a macroinitiator for the synthesis of PIPAAm-C_{60} (Fig. 1). PIPAAm-Cl, CuCl, C_{60} (1:1:3 molar ratio), and 100 ml of chlorobenzene were placed in a 300 ml round-bottom flask. After the addition of Me_6TREN (equivalent to macroinitiator), the reaction solution was refluxed for 24 h at 120 °C under argon atmosphere. Next, the solution was evaporated, tetrahydrofuran (THF) was added, and the solution was passed through a neutral alumina column to remove the catalyst and unreacted C_{60}. Finally, the PIPAAm-C_{60} was isolated by precipitation in diethyl ether and dried *in vacuo*. The two PIPAAm-C_{60}'s prepared with P-4 and P-20 were denoted as FI-4 and FI-20, respectively. Their characterization data are summarized in Table I.

D. Measurements

By ^{1}H NMR spectrometry (500 MHz, JNM-LA500, JEOL, Japan) using D_2O (Kanto Chemical, Japan), number-averaged molecular weights (M_n) of the PIPAAm-Cls were estimated from the ratio of the integral areas of the terminal methoxy protons (3.7 ppm) to that of the methine protons (3.9 ppm) of the polymer side chain (see Fig. S1 in supporting information).[20]

TABLE I. Characterization of PIPAAm-Cl and PIPAAm-C_{60}.

PIPAAm-Cl				PIPAAm-C_{60}			
Code	$10^3 M_n$ [a]	$10^3 M_n$ [b]	M_w/M_n [b]	Code	$10^3 M_n$ [b]	M_w/M_n [b]	C_{60} content (wt %)[c]
P-4	4.65	8.7	1.12	FI-4	10.3	1.13	11.3(13.4)
P-20	20.3	32.8	1.19	FI-20	33.7	1.19	2.8(3.4)

[a]Determined by ^{1}H NMR spectra in D_2O.
[b]Determined using polystyrene standards by GPC analysis in THF.
[c]Measured by DTA on the PIPAAm-Cl and the PIPAAm-C_{60}; the data in parentheses are the theoretical values based on M_n determined by ^{1}H NMR data and the C_{60}-monoadduct structure.

Additionally, M_n and polydispersity indices of the PIPAAm-Cls and PIPAAm-C_{60}'s were determined by gel permeation chromatography (GPC) (CCP-8020, Tosoh, Japan) using standard polystyrenes for calibration. THF was used as the mobile phase (at a flow rate of 1.0 ml/min at 40 °C). GPC elution profiles were obtained with a refractive index (RI) detector system (RI-8022, Tosoh) and a UV detector system (UV-8020, Tosoh, monitoring at 330 nm). To confirm the molecular assemblies of the PIPAAm-C_{60}s in water, the elution profiles for P-4, FI-4, P-20, and FI-20 were obtained from GPC measurements (Model 300 TDA, Viscotek, Texas, USA) with a RI detector (Triple Detector Array, Viscotek). Ultrapure water was used as the mobile phase (at a flow rate of 1.0 ml/min at 25 °C).

The weight percentage of C_{60} incorporated in PIPAAm-C_{60} was determined with thermogravimetric analysis (TGA) measurements (EXSTAR 6000 TG/DTA, Seiko Instruments Inc., Japan) at a heating rate of 10 °C/min under nitrogen. These measurements showed that C_{60} was thermally stable below 600 °C, whereas PIPAAm completely decomposed above 400 °C and only the C_{60} contents remained.

DLS measurements of PIPAAm-C_{60} aqueous solution were carried out on a DLS-7000 instrument (Otsuka Electronics Co., Japan) equipped with an argon ion (Ar^+) laser (488 nm) at a scattering angle of 90° at 20 °C. The concentrations of the two PIPAAm-*b*-C_{60} aqueous solutions were 5.0 mg/ml in ultrapure water. From the time correlation function of the scattering intensity, the decay time distribution function was obtained with an inverse Laplace transform program (CONTIN) provided by ALV (Germany), where the hydrodynamic radius (R_h) was determined from the Stokes–Einstein equation.

Absorbances of 5.0 mg/ml PIPAAm-Cl and 5.0 mg/ml PIPAAm-C_{60} in ultrapure water were measured at 600 nm with a UV-visible-near infrared spectrometer (V-570, Jasco, Japan) equipped with a Peltier-type thermostatic cell holder (ETC-505T, Jasco), at a heating rate of 0.2 °C/min in the temperature range from 25 to 55 °C.

III. RESULTS AND DISCUSSION

A. Identification of the synthetic PIPAAm-C_{60}

To synthesize merely a monoadduct of PIPAAm chains onto C_{60} and avoid the formation of multiple adducts, a higher ratio of C_{60} to PIPAAm-Cl (3:1) was adjusted as the experimental condition. Unreacted C_{60} was removed by dissolving the products in THF in view of the characteristics that the solubility of C_{60} is very small in THF. The GPC elution profiles for P-4 and FI-4 with both RI and UV detectors monitoring C_{60} at 330 nm are shown in Fig. 2. For P-4, there was one peak observed in the GPC curve with a RI detector but no peaks with a UV detector monitoring C_{60} at 330 nm. On the other hand, for FI-4, there was one peak in each of the GPC curves with both RI and UV detectors monitoring C_{60} at 330 nm. The two GPC elution profiles for FI-4 were nearly identical. Therefore, these results indicated

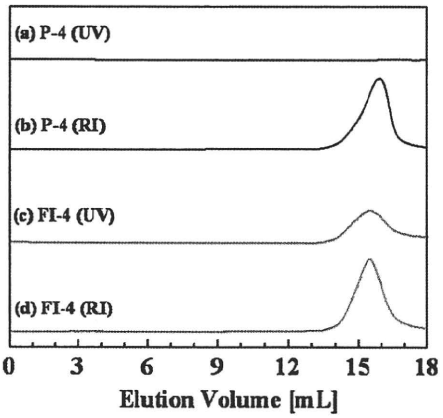

FIG. 2. (Color online) GPC curves of P-4 and FI-4 by [(a) and (c)] UV detection and [(b) and (d)] RI detection, in THF at 40 °C at a flow rate of 1.0 ml/min.

that the PIPAAm chain of FI-4 was covalently bound to a C_{60} molecule. Moreover, the GPC curve for FI-4 by RI showed the absence of multiple or broadened peaks. The M_w/M_n of FI-4 is almost the same value as P-4, as shown in Table I. These findings implied neither further ATRP-induced chain extension of PIPAAm bound onto C_{60} nor product of PIPAAms multiple adducts with a C_{60} molecule. Thus, FI-4 was confirmed to be a PIPAAm monoadduct with a C_{60} molecule. Likewise, FI-20 was also identified to be a PIPAAm monoadduct with a C_{60} molecule. The TGA profiles of P-4 and P-20 showed that the weight of the sample was negligible after 500 °C. On the other hand, the C_{60} was still stable below 600 °C. Thus, based on the weight loss of the samples at 500 °C, the C_{60} content of FI-4 and FI-20 was calculated. The experimental values for C_{60} content in both FI-4 and FI-20 from TGA roughly agreed with theoretical values estimated from the molecular weight of the PIPAAm monoadduct with C_{60}, as shown in Table I.

B. Characterization of dispersed PIPAAm-C_{60} in water below its LCST

The GPC elution profiles for P-4, P-20, FI-4, and FI-20 with a RI detector using ultrapure water as the mobile phase at 25 °C below the LCST of all samples are shown in Fig. 3. The GPC curve for P-4 showed the presence of only one

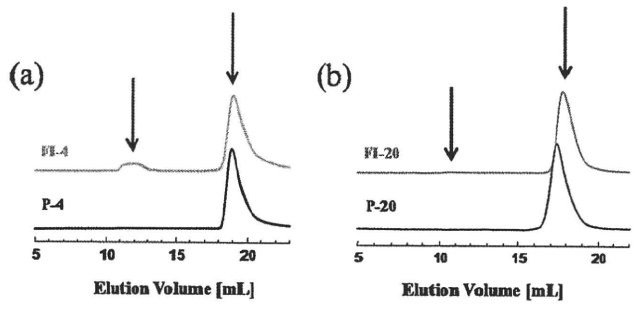

FIG. 3. (Color online) GPC curves of (a) P-4 and FI-4 and (b) P-20 and FI-20 in water. These measurements were performed at a concentration of 5.0 mg/ml at 25 °C with a flow rate of 1.0 ml/min.